PCCP

Accepted Manuscript

ROYAL SOCIETY OF CHEMISTRY

www.rsc.org/pccp

APS/123-QED

On the structure of biomedical silver-doped phosphate-based glasses from molecular dynamics simulations

Richard I. Ainsworth,[1,*] Jamieson K. Christie,[1] and Nora H. de Leeuw[1]

[1]*Department of Chemistry, University College London,*
20 *Gordon Street, London. WC1H 0AJ*

(Dated: July 6, 2014)

Abstract

First-principles and classical molecular dynamics simulations of undoped and silver-doped phosphate-based glasses with 50 mol % P_2O_5, 0-20 mol % Ag_2O, and varying amounts of Na_2O and CaO have been carried out. Ag occupies a distorted local coordination with a mean bond length of 2.5 Å and an ill-defined first coordination shell. This environment is shown to be distorted octahedral / trigonal bipyramidal. Ag-O coordination numbers of 5.42 and 5.54 - 5.71 are calculated for first-principles and classical methodologies respectively. A disproportionation in the medium-range phosphorus Q^n distribution is explicitly displayed upon silver-doping via CaO substitution, approximating $2Q^2 \rightarrow Q^1 + Q^3$, but not on silver-doping via Na_2O substitution. An accompanying increase in FWHM of the phosphorus to bridging oxygen partial pair-correlation function is strong evidence for a bulk structural mechanism associated with decreased dissolution rates with increased silver content. Experimentally, $Ag_2O \leftrightarrow Na_2O$ substitution is known to decrease dissolution and we show this to be a result of Ag's local bonding.

---

[*] n.h.deleeuw@ucl.ac.uk

I. INTRODUCTION

The doping of biomedical phosphate-based glasses (PBG) with species that have known biocidal effects, such as silver and copper ions, offers an alternative method for the treatment of infection.[1, 2] The ions can be incorporated into the glass matrix, thus providing a controlled, site-specific delivery system predicated on the degradation characteristics of the bulk glass. The bactericidal activity of doped PBG *in vitro* and *in vivo* relies on a continuous supply of the biocidal dopant into solution.[3, 4]

Ag-doped PBG has a broad spectrum of bactericidal activity against a range of bacteria[5] and associated biofilms,[3] which is linked to the effect of the Ag^+ ions on the bacterial respiratory chain and a loss of bacterial membrane integrity.[6] Increasing the concentration of Ag in the range $(P_2O_5)_{0.50}(CaO)_{0.30}(Na_2O)_{0.20-x}(Ag)_x$ ($x = 0.00 - 0.05$), leads to a decrease in glass dissolution from 1.6 to 1.1 $\mu g.mm^{-2}.h^{-1}$ across the compositional limits.[5] Similarly, for compositions $x = 0.10, 0.15$ and 0.20, dissolution rates of 1.22, 0.41 and 0.42 $\mu g.mm^{-2}.h^{-1}$ were obtained respectively.[3] Silver ion release rate is correlated to these degradation rates (0.076, 0.054 and 0.056 $ppm.h^{-1}$ respectively) corresponding to a reduction in bactericidal activity with increasing Ag^+ content. The dissolution behaviour and associated ion release is likely governed by a complex set of coupled properties such as bulk and surface structure, ionic diffusion and dissolution kinetics. In order to understand the changes in ion release rate with composition and hence optimise Ag-PBG for specific applications, a detailed understanding of the atomic structure is required.

First-principles molecular dynamics simulations using the density functional theory (DFT-MD) offer a parameter-free methodology accounting for the electronic structure of the system. These techniques have been extensively used to model PBG[7–9] and phosphosilicate glasses[10–15] allowing for an atomic-level structural characterization and calculation of electronic properties. Classical techniques based on empirical force fields[16] allow for simulations of larger cell sizes, compared to the prohibitive computational expense of DFT-MD, thus facilitating a reliable statistical description of medium-range structure.[17] Furthermore, classical MD allows for slower glass quench rates ($\sim 1 - 10$ $K.ps^{-1}$), which have been shown to improve the microscopic and macroscopic descriptions of reference amorphous systems.[18, 19] These approaches have been used to model PBG and phosphosilicate glasses and provided structures in good agreement with experiment.[20–24] The use of both classical and first-principles methodologies gives us greater confidence in our results by immediately highlighting any dependence of the results on simulation methodology.

In this work we characterise, via first-principles and classical techniques, the short- and medium-range structure of experimentally synthesised [3, 5] glass compositions with 50 mol % P_2O_5, 0-20 mol % Ag_2O, and varying amounts of Na_2O and CaO. This represents the first step to understanding dissolution phenomena in Ag-PBG, from a theoretical perspective, via the unravelling of compositional effects on bulk structure.

II. COMPUTATIONAL METHODS

Born-Oppenheimer molecular dynamics (BOMD) simulations were performed with the QUICKSTEP module[25, 26] in the CP2K code (development version 2.3.16).[27] A dual basis set was used, in which the Kohn-Sham orbitals are expanded in an atom-centered Gaussian basis set while the electronic charge density was described using an auxiliary plane-wave basis set.[28] Core electrons were described with the pseudopotential of Goedeker, Teter and Hutter (GTH)[29–31] incorporating scalar-relativistic core corrections. Valence electrons were treated with the Perdew, Burke and Ernzerhof (PBE)[32] gradient-corrected exchange-correlation functional in the double-ζ valence polarized (DZVP) basis set. The orbital transformation method[33] was employed for an efficient wavefunction optimization.

The compositional nomenclature used henceforth is, P = P_2O_5, C = CaO, N = Na_2O and A = Ag_2O, followed by the percentage molar composition for each component. The internal energy of a structurally randomised P50C30N10A10 composition is converged to $\pm 3.81\times10^{-5}$ Ry per atom at a plane-wave kinetic-energy cutoff of 700 Ry for charge density, which was therefore used in the calculations. For every self consistent field loop, the electronic gradient was converged to 1×10^{-5} Hartree. The timestep for each dynamics step was set to 1 fs with the positions, velocities and Mulliken charges[34] of all the atoms recorded for each step.

The glass generation for the first-principles (f.p.) calculations followed a standard melt-quench protocol in which atoms were initially quasi-randomly inserted into cubic simulation boxes (periodic in three-dimensions) to reproduce the experimental densities given in Table I. Two compositions (P50C40N10 and P50C30N10A10) were studied. For P50C30N10A10, a linear extrapolation of the experimental densities for ^{107}Ag and ^{109}Ag[35] was used, to reflect 50:50 isomeric abundancies. The configurations were then evolved for 3 ps in the microcanonical (NVE) ensemble. Subsequently the systems were heated to 2500 K in the canonical (NVT) ensemble and equilibrated for 30 ps. Equilibration was checked by examining the ions' actual and mean-square displacements. The systems were then cooled to 300 K at a rate of ~24 K.ps^{-1} in the NVT ensemble. The protocol followed 15 ps NVT trajectories run consecutively at 2200 K, 1900 K, 1600 K, 1300 K, 1000 K and 700 K. At 300 K the trajectory was evolved for 40 ps during which time structural and electronic data were sampled. The f.p. results in this paper are averaged over this time using every timestep. By checking the ions' mean-square displacements at 300 K, we can confirm that the model is a solid.

TABLE I: Glass compositions simulated. First-principles and classical methodologies labelled as (f.p.) and (c.) respectively.

Glass code	x	Atoms	Cell (Å)	Density (g.cm^{-3})
P50C40N10 (f.p.)	0.00	294	15.9862	2.590[36]
P50C30N10A10 (f.p.)	0.10	298	16.2615	2.846[35]
P50C40N10 (c.)	0.00	6008	43.6907	2.590[36]
P50C30N10A10 (c.)	0.10	6007	44.3763	2.846[35]
P50C30N5A15 (c.)	0.15	2999	35.0487	3.094
P50C30A20 (c.)	0.20	2999	34.9521	3.331

The classical (c.) simulations followed a similar protocol, at a reduced quench rate of ~2 K.ps^{-1}, using the formal-charge, polarizable force field shown in Table II to describe inter-atomic forces. This has previously been shown to accurately reproduce the structure of glasses in the system P_2O_5-CaO-Na_2O[8, 23, 24] and now we include an Ag-O_s two-body potential taken from Woodley *et al.*.[37] Molecular dynamics were run using the DL_POLY code[38] (version 2.20) using an Evans[39] thermostat in the NVT ensemble. In addition to the two compositions studied using first-principles methods, two compositions with higher silver content (identical to those prepared experimentally by Valappil *et al.* [3]) were simulated in order to compare to all available experimental data on dissolution rate. Three independent 3000-atom models were prepared of each of the high-Ag compositions and the results presented are averaged over all three models. The dynamics timestep was set at 0.2

fs for an accurate description of the O_s motion. The classical systems were heated to 2400 K and melted for 50 ps, after which the temperature was reduced in steps of 100 K, running each trajectory for 50 ps. Core-shell frictional damping was parameterized as $20 \leq c^2 \leq 25$ (where c is the core-shell damping coefficient which is linear in velocity) for all temperatures in the range 2400 K − 1500 K, $c^2 = 15$ at 1400 K, $c^2 = 10$ at 1300 K and $c^2 = 5$ for all temperatures in the range 1200 K − 300 K. A density correction factor of 0.950 was applied to the trajectories run at 2400 K, 2300 K and 2200 K. Likewise, a factor of 0.975 was applied at 2100 K, 2000 K and 1900 K in order to mimic thermal expansion. Since $C_{(O_s-O_s)}$ is non-zero, the simple power law expression for the dispersive energy means that $V_{(O_s-O_s)} \rightarrow -\infty$ for low r. To avoid this unphysical possibility (there is a finite probability that the system will gain sufficient kinetic energy to overcome the repulsive barrier) during the high temperature trajectories 2400K − 1500K, the potential was substituted for one of the form $V_{(O_s-O_s)} = \frac{A}{r^B}$,[40, 42] below a cut-off distance of $r_{(O_s-O_s)} = 0.952$Å. As for f.p., all classical data are averaged from the 300 K trajectory with output printed every 1 fs (to match f.p. despite the smaller timestep of 0.2 fs).

III. RESULTS AND DISCUSSION

A. Short-range order: network formers

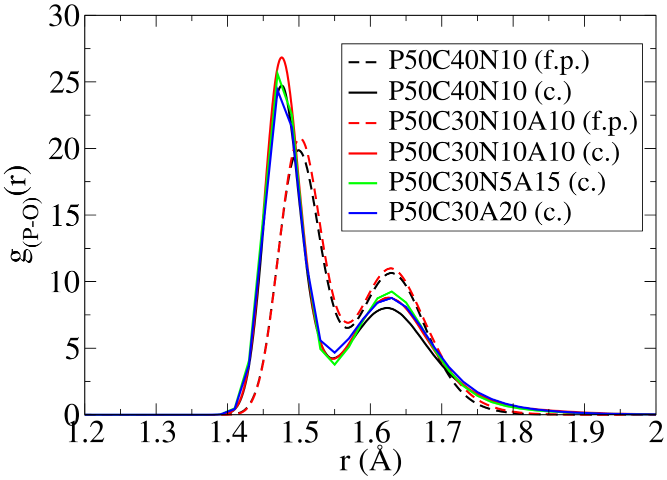

FIG. 1: P-O partial pair-correlation functions.

TABLE II: Formal charge shell-model force field used in this work, including Buckingham-type two-body, harmonic three-body and core-shell ($_{cs}$) potentials.

	$V_{ij} = Ae^{-\frac{r}{\rho}} - Cr^{-6}$		
i-j	A(eV)	ρ (Å)	C (eV.$Å^6$)
P-O_s[23]	1020.0000	0.343220	0.0300
O_s-O_s[41]	22764.30	0.149000	27.88
Na-O_s[42]	56465.3453	0.193931	0.00
Ca-O_s[42]	2152.3566	0.309227	0.099440
Ag-O_s[37]	962.197	0.300000	0.00
	$V_{ijk} = \frac{1}{2}k_{3b}(\theta - \theta_0)^2$		
i-j-k	k_{3b}(eV.rad^{-2})	θ_0(°)	
O_s-P-O_s[23]	3.3588	109.470000	
P-O_s-P[23]	7.6346	141.179333	
	$V_{ij} = \frac{1}{2}k_{cs}r^2$		
i-j	k_{cs}(eV.$Å^{-2}$)	O_c (e)	O_s (e)
O_c-O_s[41]	74.92	+0.8482	-2.8482

The glass network for each composition is made up of inter-linked PO_4 tetrahedra. Figure 1 displays the partial pair-correlation functions $g_{(P-O)}$ (r) between $1.2 - 2.0$ Å (within the first coordination shell). Both methodologies distinguish between the longer phosphorus to "bridging" oxygen bonds (P-BO), with $g_{(P-O)}$ (r) peaks centered between $1.62 - 1.63$ Å and the shorter phosphorus to "non-bridging" oxygen bonds (P-NBO), centered between $1.48 - 1.50$ Å. The slight overestimation from DFT-MD results are likely due to GGA underbinding and hence overestimating bond lengths. Pickup *et al.*[36] used neutron diffraction (ND) and ^{31}P magic angle spinning nuclear magnetic resonance (MAS NMR) spectroscopy to probe the structure of P50C40N10. The structural parameters were obtained via simulation of the reciprocal-space data and conversion of the results to real space via Fourier transform (to make comparison to the correlation function from ND). Their results give $r_{(P-BO)} = 1.60$ Å ±0.02 Å and $r_{(P-NBO)} = 1.49$ Å ±0.02 Å. The classical simulations reproduce these bond lengths well (see Table III), as does the glass simulated by first-principles techniques. For the Ag-PBG composition (P50C30N10A10) comparison is made to data from ND experiments,[35] using samples enriched with both ^{107}Ag and ^{109}Ag. Experimentally, it was shown that for both silver isotopes, $\mathrm{r_{(P-BO)}} = 1.60$ Å ±0.01 Å and $\mathrm{r_{(P-NBO)}} = 1.48$ Å ±0.01 Å. From the current work, $\mathrm{r_{(P-BO)}}$ is slightly overestimated by both methodologies, with an accurate representation of $\mathrm{r_{(P-NBO)}}$ in P50C30N10A10 (c.). It can be seen from these results that the addition of Ag to the glass, even at high-Ag content, has no effect on $\mathrm{r_{(P-BO)}}$ and $\mathrm{r_{(P-NBO)}}$.

The disorder parameters σ_{ij}, measuring static and thermal disorder, from the pair functions for P-BO and P-NBO are a measure of the width of the relevant pair-correlation peak. In experimental work, σ_{ij} are derived from Q-space simulation using Equation 1:

$$\mathrm{p(Q)_{ij}} = \frac{\mathrm{N_{ij}w_{ij}}}{\mathrm{c_j}} \frac{\sin \mathrm{QR_{ij}}}{\mathrm{QR_{ij}}} \exp\left[\frac{-\mathrm{Q}^2\sigma_{\mathrm{ij}}^2}{2}\right], \qquad (1)$$

where $\mathrm{p(Q)_{ij}}$ is the pair function in reciprocal space, $\mathrm{N_{ij}}$, $\mathrm{R_{ij}}$ and σ_{ij} are the coordination number, atomic separation and disorder parameter (referred to as $\sigma_{\mathrm{ij}}^{\mathrm{ND}}$ from this point onwards), respectively, of atom i with respect to j. $\mathrm{c_j}$ is the concentration of atom j and $\mathrm{w_{ij}}$ is the weighting factor, given by $\mathrm{w_{ij}} = 2\mathrm{c_i c_j b_i b_j}$ if $\mathrm{i} \neq \mathrm{j}$ and $\mathrm{w_{ij}} = \mathrm{c_i^2 b_i^2}$ if $\mathrm{i} = \mathrm{j}$ (where b represents the coherent scattering length). From the current work the full-width-half-maximum (FWHM) values of the decomposed partial-pair correlation functions $\mathrm{g_{(P-O)}}$ (f.p.) have been calculated. Making the assumption that $\mathrm{g_{(P-NBO)}}$ (r) and $\mathrm{g_{(P-BO)}}$ (r) are normally distributed (for the first coordination sphere) gives, $\mathrm{FWHM_{ij}^{f.p.}} = 2\sqrt{2\ln 2}\sigma_{\mathrm{ij}}^{\mathrm{f.p.}}$, from which $\sigma_{\mathrm{ij}}^{\mathrm{f.p.}}$ are derived.

Comparison of the compositional trends in simulated $\sigma_{\mathrm{(P-BO)}}^{\mathrm{ND}}$ and $\sigma_{\mathrm{(P-NBO)}}^{\mathrm{ND}}$ from ND experimental work, with trends in $\sigma_{\mathrm{ij}}^{\mathrm{f.p.}}$ values of $\mathrm{g_{(P-BO)}}$ and $\mathrm{g_{(P-NBO)}}$ from this work, is presented in Table IV. Experimentally, it is noted that P-BO disorder increases upon 10 mol % Ag-doping from $\sigma_{\mathrm{(P-BO)}}^{\mathrm{ND}} = 0.048$Å to $\sigma_{\mathrm{(P-BO)}}^{\mathrm{ND}} = 0.060$Å. In our calculations, $\sigma_{\mathrm{(P-BO)}}^{\mathrm{f.p.}}$ increases from 0.048 Å in P50C40N10 (f.p.) to 0.052 Å in P50C30N10A10 (f.p.) in good agreement with ND. $\sigma_{\mathrm{(P-NBO)}}^{\mathrm{ND}}$ increases from 0.036 Å to 0.060 Å with the inclusion of silver. No significance can be attributed to the 0.001 Å increase upon doping, for the associated $\mathrm{g_{(P-NBO)}}$ FWHM values from this work. However, ND and f.p. $\sigma_{\mathrm{(P-NBO)}}$ are in reasonable agreement for P50C40N10. Increases in disorder parameters are linked to changes in local

TABLE III: Selected partial pair-correlation peak distances ($r_{(X-X)}$ (Å)). Experimental data obtained via neutron (ND) and X-ray (XRD) diffraction, are given for comparison. $^{(*)}$ Further analysis of Ag-O average distances ($\bar{r}_{(Ag-O)}$) given in Table VII.

	P50C40N10			P50C30N10A10			P50C30N5A15	P50C30A20
	f. p.	c.	ND[36]	f. p.	c.	ND & XRD[35]	c.	c.
$r_{(P-NBO)}$	1.50	1.48	1.49 ±0.02	1.50	1.48	1.48 ±0.01	1.48	1.47
$r_{(P-BO)}$	1.63	1.62	1.60 ±0.02	1.63	1.62	1.60 ±0.01	1.63	1.63
$r_{(O-O)}$	2.56	2.54	2.52 ±0.02	2.57	2.55	2.51 ±0.01	2.55	2.55
$r_{(P-P)}$	2.94	3.02	2.93 ±0.02	2.96	3.03	2.93 ±0.01	3.03	3.03
$r_{(Ca-O)}$	2.35	2.33	2.34 ±0.02	2.34	2.31	2.38 ±0.01	2.32	2.32
$r_{(Na-O)}$	2.38	2.36	2.33 ±0.02	2.37	2.34	2.33 ±0.01	2.36	-
$r_{(Ag-O)}{}^{(*)}$	–	–	–	2.37	2.29	2.28,2.51,2.73 ±0.03	2.27	2.29

bonding environments and, in turn, linked to a disproportionation in the medium-range structure[35] (see sub-section III D).

Figure 2 displays the partial pair-correlation functions for O-O and P-P. It can be seen that there are no significant compositional or methodological dependencies on the O-O distributions. However, the second coordination shell at ∼3.2 Å, is stronger for first-principles results in conjunction with stronger peaks in the O-P-O (f.p.) angular distribution function (ADF) (see Figure 3), when compared to classical results. These differences are most likely a feature of the parameterization of the force field used in this work. The first peak in $g_{(P-P)}$ (r) shifts from a peak-centered position of 2.93 Å in P50C40N10 (f.p.) to 2.95 Å in P50C30N10A10 (f.p.) and sharpens considerably. This is accompanied by an increase of approximately 4% in the peak-centered positions of $P_{(P-O-P)}(\theta)$ from 125° in P50C40N10 (f.p.) to 129° in P50C30N10A10 (f.p.), thus indicating a possibly significant structural change upon doping the glass via substitution of CaO for Ag_2O. This is further discussed in Section III C, in relation to the coordination environment of Ag. The classical results do not corroborate these features due to the inclusion of a P-O_s-P three-body potential, as previously discussed.[23]

TABLE IV: Full-width-half-maximum (FWHM) values from the decomposed partial-pair correlation functions $g_{(P-O)}$ (f.p.) and disorder parameters $\sigma_{ij}^{f.p.}$ (standard deviation under the assumption that $g_{(P-BO)}$ and $g_{(P-NBO)}$ are normally distributed). Disorder parameters σ_{ij}^{ND} from Q-space simulation (see Equation 1) of experimental ND diffraction data.[35, 36]

i-j	Model	$FWHM_{ij}^{f.p.}$ (Å)	$\sigma_{ij}^{f.p.}$ (Å)	σ_{ij}^{ND} (Å)
P-BO	P50C40N10 (f.p.)	0.114	0.048	0.048 ±0.01[36]
P-BO	P50C30N10A10 (f.p.)	0.123	0.052	0.060 ±0.01[35]
P-NBO	P50C40N10 (f.p.)	0.075	0.032	0.036 ±0.01[36]
P-NBO	P50C30N10A10 (f.p.)	0.076	0.032	0.060 ±0.01[35]

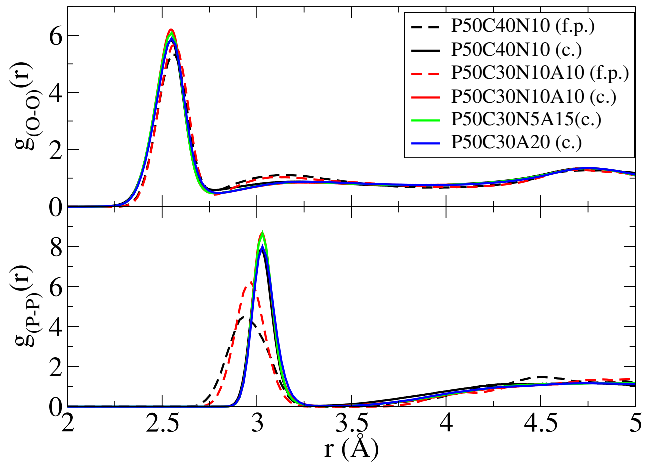

FIG. 2: O-O and P-P partial pair-correlation functions.

B. Short-range order: network modifiers

The partial pair-correlation functions for the network modifiers (Me) Ca, Na and Ag, with respect to oxygen, are given in Figure 4. The classical and first-principles distributions are in good agreement. For both methodologies, the normalised peak intensities for Ca-O and Na-O increase upon Ag-doping, with the consequence of decreasing the FWHM in all cases. The ill-defined first minimum for $g_{(Ag-O)}$ (r) from P50C30N10A10 (f.p.) (2.7 Å – 3.2 Å), suggests a distorted first coordination shell (however the 298 atom model also leads to poorer statistical sampling and increased signal noise). This in turn narrows the bond

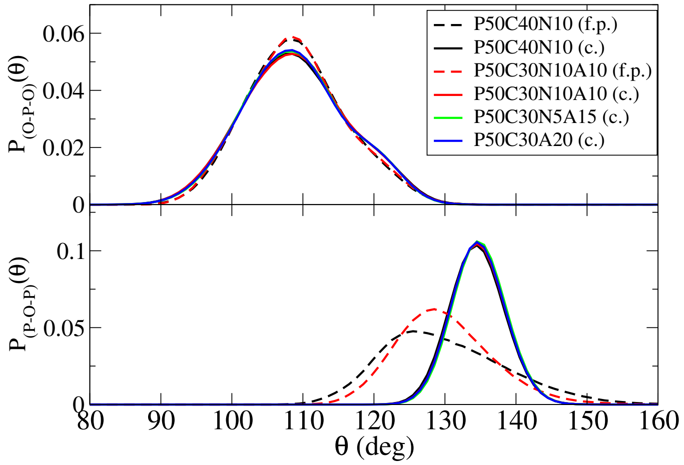

FIG. 3: O-P-O and P-O-P angular distribution functions.

length distributions for the other modifiers Ca and Na due to geometrical constraints.

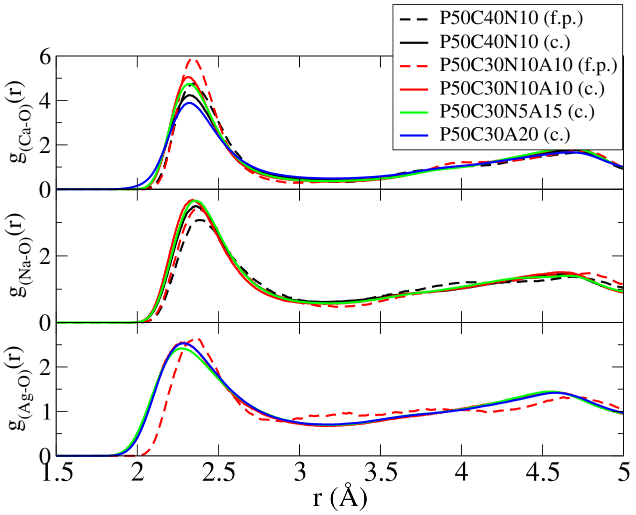

FIG. 4: Ca-O, Na-O and Ag-O partial pair-correlation functions.

The peaks of the distributions $g_{(Me-O)}$ (r) from classical simulations are centered on bond lengths 0.05 − 0.15 Å below the peaks of respective compositions from first-principles results, consistent with comparison of a structure derived from a well-parameterized force field and an underbinding GGA calculation. As with the short-range structure of the network-forming species, the network-modifier bond lengths are in good agreement with available

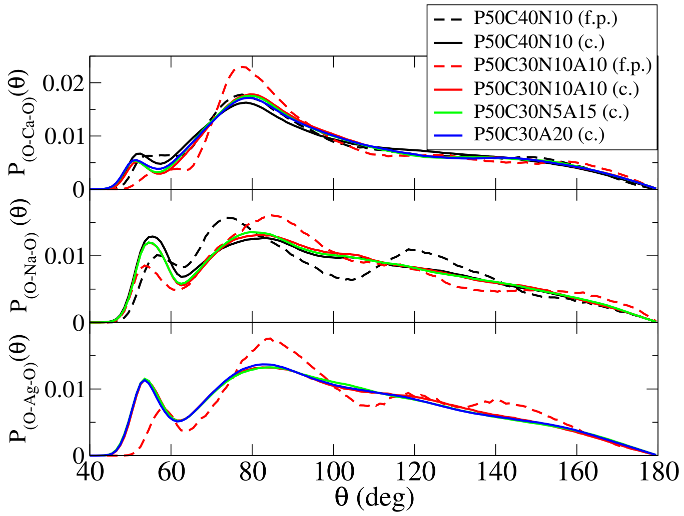

FIG. 5: O-Ca-O, O-Na-O and O-Ag-O angular distribution functions. Me-O cut-offs taken as first minimum of respective radial distribution functions.

experimental data (see Table III).

Figure 5 displays the ADFs for the three-body systems O-Me-O. For the O-Ca-O system there is a strong localisation of bond angles at ∼80° and a significant contribution of angles up to 150°, consistent with a distorted octahedral coordination, as found in other Ag-free PBG.[23] As also indicated, by a large normalised peak intensity in $g_{(\mathrm{Ca-O})}$ (r) and first minimum located at 3 Å, the O-Ca-O distribution for P50C30N10A10 (f.p.) displays increased intensity at ∼80° when compared to P50C40N10 (f.p.) (a dopant-dependent feature also seen in classical results). This indicates that the Ca ions in this model bond in a more symmetric octahedron which is likely linked to the presence of two further modifier species in the composition. A secondary set of peaks of lower intensity in the range $50 - 65°$ are attributed to intra-tetrahedral environments, where both oxygens are bonded to a common phosphorus atom.[23, 43] The ADFs for O-Na-O show significant compositional dependence for f.p. models. P50C40N10 (f.p.) has peaks at 57°, 75° and 120° compared to the stronger octahedral coordination of P50C30N10A10 (f.p.) with peaks at 52°, 84° and ∼ 160°. Results from the classical simulations show no significant compositional dependence although there is increased intra-tetrahedral contribution. The O-Ag-O distribution for P50C30N10A10 (f.p.) has three dominant peaks centered at 54°, 84°, 118° with a shoulder feature at ∼140°, suggesting a distorted bonding environment (representative Ag environment shown in Figure

6). The classical results show very good agreement, with a slightly smoother distribution of O-Ag-O bond-angles (likely a statistical effect coupled with a differing description of inter-atomic forces). Peaks from the latter are centered on 54° and 84° with a shoulder at ∼120° (see Figure 5).

C. Modifier coordination

Both compositions studied contain a variety of local environments. f.p. results commonly show more highly resolved angular contributions, which may be a product of poor statistical sampling, or may reflect the highly accurate description of inter-atomic forces. As previously shown from ADFs, Ca displays a distorted octahedral coordination environment and this is confirmed by coordination numbers ($\eta_{(\mathrm{Ca-O})}$) of 6.91 and 6.57 for P50C40N10 (f.p.) and P50C30N10A10 (f.p.) respectively (see Table V). This 0.34 decrease in $\eta_{(\mathrm{Ca-O})}$ further indicates increased octahedral symmetry upon 10 mol % Ag-doping. f.p. results show $\eta_{(\mathrm{Na-O})} = 6.07$ reducing to $\eta_{(\mathrm{Na-O})} = 5.85$ when the glass is doped. These results are similar to previous MD simulations of ultra-phosphate PBG compositions.[23] For f.p. results, $\eta_{\mathrm{Ag-O}} = 5.42$ at a cut-off of 3.20 Å. As previously stated, there is an ill-defined minimum in $\mathrm{g}_{(\mathrm{Ag-O})}$ (r) and the dependence of $\eta_{(\mathrm{Ag-O})}$ on Ag-O cut-off (Ag-O$_{(\mathrm{cut})}$) is given in Table VI, ranging from $\eta_{(\mathrm{Ag-O})} = 3.71$ at Ag-O$_{(\mathrm{cut})} = 2.80$ Å to $\eta_{(\mathrm{Ag-O})} = 6.55$ at Ag-O$_{(\mathrm{cut})} = 3.40$ Å.

Several X-ray absorption Near Edge Structure (XANES) studies of $0-20$ mol% Ag PBG, have shown the shape and position of the Ag K-edge spectra to be identical to the reference material Ag_2SO_4.[3, 35, 44] From these studies, the authors have concluded that the Ag ion in Ag-PBG has a structural environment very similar to that of Ag_2SO_4. Figure 6 shows an example Ag ion coordination environment from the P50C30N10A10 (f.p.) model along with the local coordination environment of Ag^{I} in Ag_2SO_4 in the upper and lower panels respectively.[45] Both structures show a distorted octahedral symmetry, providing further evidence of the similarities in Ag local ordering.

Moss *et al.*[35] have previously conducted neutron diffraction with isotopic substitution (NDIS) using P50C30N10A10 samples enriched with ^{107}Ag and ^{109}Ag isotopes. This allows for the simplification of complex correlations[46] (assuming each sample has identical composition and structure) by the application of difference function methods.[47, 48] They showed[35] that the Ag-O correlation has three components in the first coordination shell at

TABLE V: Modifier & dopant coordination environments for f.p. and c. simulations. Coordination numbers (η) with Ca-O, Na-O and Ag-O cut-offs set at 3.22 (f.p.)/ 3.25 (c.) Å, 3.15 (f.p.)/ 3.15 (c.) Å and 3.20 (f.p.) / 3.15 (c.) Å respectively (bond lengths at first minima of respective partial pair-correlation functions). η decomposed into BO and NBO contributions.

	P50C40N10 (f.p.)	P50C30N10A10 (f.p.)
Atomic Pair	η	η
Ca-O	6.91	6.57
Ca-BO	0.52	0.48
Ca-NBO	6.39	6.09
Na-O	6.07	5.85
Na-BO	0.99	0.85
Na-NBO	5.08	5.00
Ag-O	–	5.42
Ag-BO	–	0.82
Ag-NBO	–	4.60

	P50C40N10 (c.)	P50C30N10A10 (c.)	P50C30N5A15 (c.)	P50C30A20 (c.)
Atomic Pair	η	η	η	η
Ca-O	6.79	6.44	6.57	6.51
Ca-BO	0.65	0.49	0.47	0.73
Ca-NBO	6.14	5.95	6.10	5.78
Na-O	6.48	6.02	6.26	–
Na-BO	1.43	1.18	1.29	–
Na-NBO	5.05	4.84	4.98	–
Ag-O	–	5.54	5.62	5.71
Ag-BO	–	0.98	1.04	1.05
Ag-NBO	–	4.56	4.58	4.65

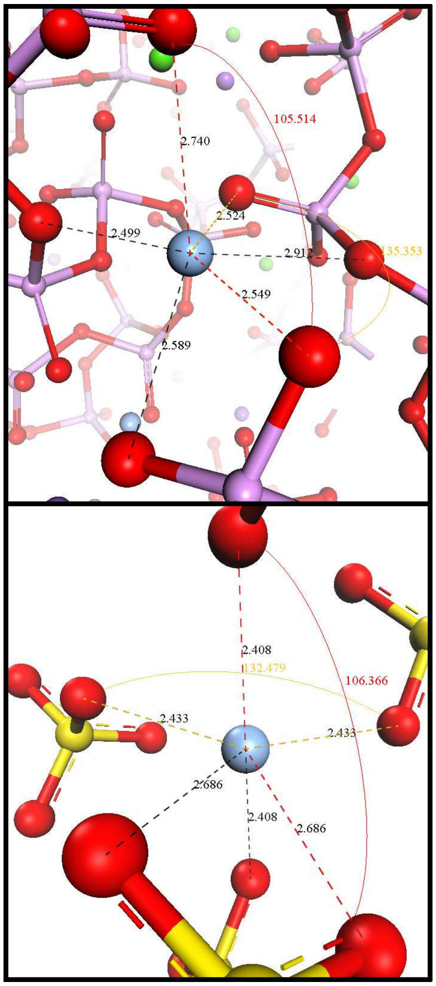

FIG. 6: Example Ag coordination environment in P50C30N10A10 (f.p.) (upper panel) and crystalline Ag_2SO_4 - space group $Fddd$, No. 70[45] (lower panel). Common distorted octahedral geometry and in-plane intra-tetrahedral coordination.

2.28 Å, 2.51 Å and 2.73 Å with coordination numbers of 2.1, 2.7 and 1.1 respectively. $g_{(\mathrm{Ag-O})}$ (r) from the current work (see Table 4 for peak position) displays a unimodal distribution within the first coordination sphere, for both methodologies, with no evidence for multiple resolved peaks. Table VII shows a direct comparison of the Ag-O mean bond lengths for both methodologies, $\bar{\mathrm{r}}^{\mathrm{f.p.}}_{(\mathrm{Ag-O})}$ and $\bar{\mathrm{r}}^{\mathrm{c.}}_{(\mathrm{Ag-O})}$, in P50C30N10A10, as a function of Ag-$\mathrm{O}_{(\mathrm{cut})}$ for the first coordination sphere. The experimental value of $\bar{\mathrm{r}}^{\mathrm{NDIS}}_{(\mathrm{Ag-O})}$ = 2.47 Å ±0.07 Å[35] is derived using the published bond lengths weighted according to coordination number. $\bar{\mathrm{r}}^{\mathrm{f.p.}}_{(\mathrm{Ag-O})}$ and $\bar{\mathrm{r}}^{\mathrm{c.}}_{(\mathrm{Ag-O})}$ provide a more direct comparison to experiment, compared to the peak centered position of $g_{(\mathrm{Ag-O})}$ (r), due to the fact that the partial pair-correlation does not decay to zero at the limit of the first coordination sphere, resulting in the deviation of peak

TABLE VI: Silver to oxygen coordination numbers (η) as a function of Ag-O cut-off for P50C30N10A10 (f.p.).

	2.80 Å	2.90 Å	3.00 Å	3.10 Å	3.20 Å	3.30 Å	3.40 Å
Atomic Pair	η	η	η	η	η	η	η
Ag-O	3.71	4.07	4.47	4.92	5.42	5.98	6.55
Ag-BO	0.22	0.33	0.47	0.63	0.82	1.05	1.29
Ag-NBO	3.49	3.74	4.00	4.29	4.60	4.93	5.26

TABLE VII: Mean silver to oxygen bond lengths ($\bar{r}_{(Ag-O)}$) in first coordination sphere as a function of Ag-O cut-off for P50C30N10A10 (f.p.) and P50C30N10A10 (c.) Average bond length from experiment $\bar{r}^{NDIS}_{(Ag-O)}$ = 2.47 Å ±0.07 Å.[35]

	2.90 Å	2.95 Å	3.00 Å	3.05 Å	3.10 Å	3.15 Å	3.20 Å	3.25 Å	3.30 Å
$\bar{r}^{f.p.}_{(Ag-O)}$ (Å)	2.46	2.47	2.49	2.50	2.53	2.54	2.57	2.58	2.61
$\bar{r}^{c.}_{(Ag-O)}$ (Å)	2.41	2.44	2.47	2.50	2.53	2.55	2.58	2.61	2.64

centered values from the mean bond length. $\bar{r}^{f.p.}_{(Ag-O)}$ and $\bar{r}^{c.}_{(Ag-O)}$ range from 2.46 – 2.61 Å and 2.41 – 2.64 Å respectively, across the range Ag-$O_{(cut)}$ = 2.90 Å – 3.30 Å, in good agreement with experiment.

Figure 6 facilitates a more detailed assignment of peaks in the P50C30N10A10 (f.p.) O-Ag-O ADF from Figure 5. The peak at 54° corresponds to intra-tetrahedral bonding as evidenced in the example environment shown. This distorted octahedral geometry also shows further in plane angles at 77°, 135° and 147° contributing to the peak at 84° and shoulder feature at ∼140° in the ADF. Furthermore, Ag-O first-coordination environments with 5-coordinated distorted trigonal bipyramidal geometries were observed, constituting contributions to the ADF peaks centered on 84° and 118°.

$\eta_{(Me-O)}$ values from classical simulations (c.) of P50C30N10A10 are given in the lower half of Table V with amended cut-offs to reflect differing first minima in $g_{(Me-O)}$ (r) (c.). Direct comparison to f.p. results shows good agreement for $\eta_{(Ca-O)}$ and $\eta_{(Na-O)}$ with similar decompositions for BO and NBO. Upon 10 mol % Ag-doping $\eta_{(Ca-O)}$ (c.) and $\eta_{(Na-O)}$ (c.) decrease by 0.35 and 0.46 respectively, compared to decreases of 0.34 (f.p.) and 0.22

(f.p.) respectively. $\eta_{(\mathrm{Ag-O})} = 5.54$ (c.) at Ag-O$_{(\mathrm{cut})} = 3.15$ Å, which compared to similar cut-off values for (f.p.) results given in Table VI, and 5.62 and 5.71 for high-Ag content compositions, is in good agreement.

D. Medium-range order

The larger simulation models used in classical methods facilitate a more statistically sound analysis of the medium-range structure, providing insight into compositionally dependent structural trends at these length scales. Thus, only results from the classical simulations are presented in this section. Moss *et al.*[35] have inferred that a disproportionation in the medium-range $\mathrm{Q^n}$ distribution occurs upon CaO substitution with $\mathrm{Ag_2O}$ for the compositions studied here. The authors, using a simple bond-order model, show that an increase in $\sigma_{(\mathrm{P-BO})}$ and static disorder of P-NBO implies a disproportionation in the network structure. Valappil *et al.*[3] explicitly showed, via ^{31}P MAS NMR spectral analysis, that the substitution of $\mathrm{Na_2O}$ with $\mathrm{Ag_2O}$, for the compositions $\mathrm{(P_2O_5)_{0.50}(CaO)_{0.30}(Na_2O)_{0.20-x}(Ag_2O)_x}$ (x = 0.00, 0.10, 0.15 and 0.20), leads to a disproportionation of $\mathrm{Q^2}$ units approximating the relation $\mathrm{2Q^2 \rightarrow Q^1 + Q^3}$, for $\mathrm{x} \geq 0.10$.

The phosphorus Q^n distributions from classical simulations are given in Table VIII. P50C40N10 (c.) comprises 79.7% $\mathrm{Q^2}$, 9.9% $\mathrm{Q^1}$ and 9.7% $\mathrm{Q^3}$ from our simulations compared to 96% $\mathrm{Q^2}$ and 4% $\mathrm{Q^1}$ from experiment.[36] Similar levels of agreement with experiment are found for classical MD derived phosphate,[23] phosphosilicate[20] and sodium silicate[42, 49] glasses.

The potential reasons for discrepancies between theoretical and experimental $\mathrm{Q^n}$ distributions are wide ranging and include modal assumptions when deconvoluting experimental NMR signals. From the theory side, Stebbins[50] found that both an increase in glass transition temperature (known to be higher in theoretical simulations than experiment) and higher field strength modifiers caused the disproportionation reactions, $\mathrm{2Q^n \rightarrow Q^{n-1} + Q^{n+1}}$ (for n = 1, 2 and 3), in silicate glasses. The discrepancies in $\mathrm{Q^1}$, $\mathrm{Q^2}$ and $\mathrm{Q^3}$ proportions for P50C40N10 (c.) from the current work (compared to experiment) may relate to fictive temperatures that are in excess of experiment (further limitations with MD methods are discussed by Pota *et al.*[51]). In any case, we are interested in the *trends* of the Q^n distribution on Ag-doping, and the absolute values are less important.

TABLE VIII: Q^n species distribution (%) (for phosphorus with respect to oxygen) and network connectivity (NC). Experimental data (expt.) from fitting to ^{31}P MAS NMR spectra.[36]

	Q^0	Q^1	Q^2	Q^3	Q^4	NC
P50C40N10 expt.	0.0	4.0	96.0	0.0	0.0	1.96
P50C40N10 (c.)	0.6	9.9	79.7	9.7	0.1	1.99
P50C30N10A10 (c.)	0.4	10.9	78.0	10.6	0.1	1.99
P50C30N5A15 (c.)	0.2	9.0	82.0	8.8	0.0	1.99
P50C20A20 (c.)	0.3	9.3	81.1	9.3	0.1	2.00

For P50C30N10A10 (c), Q^2 reduces to 78% with concomitant rises in Q^1 and Q^3, approximating the relation found by Valappil and co-workers,[3] but we do not observe this disproportionation occurring at $>$ 10 mol % Ag_2O (Table VIII).

Network connectivity (NC), defined as the mean number of BO within the first coordination shell of phosphorus summed over all P atoms, is 1.99 - 2.00 for all simulated compositions. This is very close to the value of 2.0 expected theoretically and found experimentally.[36]

E. Atomic charges

The mean atomic charges obtained by Mulliken population analysis are given in Table IX. These are summed over all timesteps of the 300 K trajectory from f.p. models. No significant changes are noted upon Ag-doping with net phosphorus charges of +0.760 and +0.766 for P50C40N10 (f.p.) and P50C30N10A10 (f.p.) respectively. It should be noted that Mulliken charges are calculated by determining the electron population of each atom as defined by the basis functions and absolute values are therefore dependent on the choice of basis set. Hence, although the partition of the electronic density is somewhat arbitrary, we use Mulliken charge analysis for direct comparison to previous work, and for its relative ease of implentation. We are not attempting any detailed quantitative analysis of the atomic charges.

The electronic states and chemical bonding in phosphate glass have previously been

TABLE IX: Mean Mulliken charges for all atomic species X ($Q_{(X)}$) in P50C40N10 (f.p.) and P50C30N10A10 (f.p.).

	P50C40N10 (f.p.)	P50C30N10A10 (f.p.)
$Q_{(P)}$	+0.760	+0.766
$Q_{(O)}$	−0.459	−0.453
$Q_{(BO)}$	−0.384	−0.384
$Q_{(NBO)}$	−0.497	−0.488
$Q_{(Ca)}$	+1.146	+1.130
$Q_{(Na)}$	+0.810	+0.791
$Q_{(Ag)}$	—	+0.540

studied by Kowada *et al.*[52] using the DV-Xα cluster method. For the charge-balanced P_4O_{10} cluster the net charge on phosphorus was found to be +1.31 using Mulliken population analysis. In the context of the other atoms in this study, the phosphorus atoms have a covalent interaction with the surrounding oxygens. The mean oxygen atomic charges have been deconvoluted into BO and NBO, with the NBO displaying increased ionic character with net charges of −0.497 and −0.488 for PBG and Ag-PBG respectively. Mean BO charges are found to be +0.113 and +0.104 higher due to the presence of two covalently bonded phosphorus atoms in their first coordination sphere. These changes are in good agreement with the relation $Q_{(BO)} = Q_{(NBO)} + 0.12$ for the cluster P_4O_{10}.[52] All modifier ions show increased ionic character compared to the network formers. XANES analysis conducted by Ahmed *et al.*[44] has shown silver to be in the Ag^I oxidation state for a series of Ag-PBG. The effective ionic radii for six-coordinate Ag^I and Na^I are 1.15 and 1.02 Å respectively,[53] suggestive of a higher effective charge for Na^I compared to Ag^I, as corroborated by $Q_{(Na)} = +0.791$ and $Q_{(Ag)} = +0.540$ for P50C30N10A10 (f.p.).

IV. DISCUSSION AND CONCLUSIONS

We have investigated the structures of biomedically relevant glasses with 50 mol % P_2O_5, 0-20 mol % Ag_2O and varying amounts of Na_2O and CaO, using first-principles (f.p.) and classical (c.) molecular dynamics simulations. Good agreement is found between the results from c. simulations (using a force field that was previously developed within our group[23]) and the high level f.p. reference calculations. The c. methodology outperforms f.p. in reproducing some key structural features, when compared to experimental data, such as P-O bond distances. The Ag ion is noted to have little effect on short-range order.

Ag itself has a distorted octahedral and trigonal bipyramidal structure with an ill defined first-coordination shell where the Ag-O coordination number is approximately 5.5 and the bond length is ~ 2.5Å, implying that Ag is acting as a network modifier.

At low Ag content, and for $Ag_2O \leftrightarrow CaO$ substitution, there is experimental evidence for a disproportionation in the medium-range Q^n distribution for phosphorus upon doping, following the relation $2Q^2 \rightarrow Q^1 + Q^3$, which we also find in simulation. An increase in P-BO bond disorder (as seen in experiment[35, 36]) from f.p. results on 0 and 10 mol % Ag_2O compositions, further supports this feature. These structural changes are of likely consequence in the observed decrease in dissolution rates with increased Ag mol%. However, we do not see this disproportionation at higher Ag contents when Ag_2O is substituted for Na_2O.

In fact, it is rather difficult to disentangle the precise effect of Ag on the glass dissolution because of the different substitutions employed in past experiments. We cannot say with certainty whether the composition dependence of the disproportionation reaction is due to differing Ag content, or to differences in the moiety for which Ag_2O is substituted.

What is perfectly clear from experiment is that when Ag_2O is substituted for Na_2O, the dissolution rate goes down. Our simulations show clearly that this is due to differences in the local bonding. Ag has a field strength intermediate between Na and Ca, which is reflected in the intermediate number of bridging oxygen atoms to which Ag is bonded (Table V). The experimental implication is that Ag is bonded to more parts of the phosphate network than Na, and that its substitution for Na strengthens the glass network through greater cross-linking. Although we show that Ag has a lower coordination number than Na, it seems that this is less important than the value of its field strength. Although it is doubtful that 50 mol % P_2O_5 glasses have short phosphate chains in the way that lower-phosphate content glasses do, the effect is similar to Ca bonding together more phosphate chains than Na in low-phosphate glasses, as we have previously identified [24].

ACKNOWLEDGMENTS

The authors would like to thank the Engineering and Physical Sciences Research Council (United Kingdom) EPSRC(GB) (EP/J008095) for funding. Via our membership of the UK's HPC Materials Chemistry Consortium, which is funded by EPSRC (EP/F067496), this work made use of the facilities of HECToR, the UK's national high-performance computing service, which is provided by UoE HPCx Ltd. at the University of Edinburgh, Cray Inc. and NAG Ltd., and funded by the Office of Science and Technology through EPSRC's High End Computing Programme. We are grateful to Devis Di Tommaso for helpful discussions.

[1] R. Sheridan, P. J. Doherty, T. Gilchrist, and D. Healy, Journal of Materials Science-Materials in Medicine **6**, 853-856 (1995).

[2] T. Gilchrist, D. M. Healy, and C. Drake, Biomaterials **12**, 76-78 (1991).

[3] S. P. Valappil, D. M. Pickup, D. L. Carroll, C. K. Hope, J. Pratten, R. J. Newport, M. E. Smith, M. Wilson, and J. C. Knowles, Antimicrobial Agents and Chemotherapy **51**, 4453-4461 (2007).

[4] A. M. Mulligan, M. Wilson, and J. C. Knowles, Biomaterials **24**, 1797-1807 (2003).

[5] I. Ahmed, D. Ready, M. Wilson, and J. C. Knowles, Journal of Biomedical Materials Research Part A **79A**, 618-626 (2006).

[6] C. P. Randall, L. B. Oyama, J. M. Bostock, I. Chopra, and A. J. Oneill, Journal of Antimicrobial Chemotherapy **68**, 131-138 (2013).

[7] E. Tang, D. Di Tommaso, and N. H. de Leeuw, Advanced Engineering Materials **12**, B331-B338 (2010).

[8] D. Di Tommaso, R. I. Ainsworth, E. Tang, and N. H. de Leeuw, Journal of Materials Chemistry B **1**, 5054 (2013).

[9] J. K. Christie, R. I. Ainsworth, and N. H. de Leeuw, Biomaterials **35**, 6164-6171 (2014).

[10] A. Tilocca, N. H. de Leeuw, and A. N. Cormack, Physical Review B **73**, 104209 (2006).

[11] A. Tilocca, Physical Review B **76**, 224202 (2007).

[12] A. Tilocca, A. N. Cormack, and N. H. de Leeuw, Faraday Discussions **136**, 45-55 (2007).

[13] J. K. Christie, and A. Tilocca, Advanced Engineering Materials **12**, B326-B330 (2010).

[14] A. Tilocca, Journal of Materials Chemistry **20**, 6848-6858 (2010).

[15] J. K. Christie, A. Pedone, M. C. Menziani, and A. Tilocca, The Journal of Physical Chemistry B **115**, 2038-2045 (2011).

[16] A. Pedone, The Journal of Physical Chemistry C **113**, 20773-20784 (2009).

[17] A. Tilocca, The Journal of Chemical Physics **129**, 084504 (2008).

[18] K. Vollmayr, W. Kob, and K. Binder, The Journal of Chemical Physics **105**, 4714-4728 (1996).

[19] K. Vollmayr, W. Kob, and K. Binder, Physical Review B **54**, 15808-15827 (1996).

[20] A. Tilocca, A. N. Cormack, and N. H. de Leeuw, Chemistry of Materials **19**, 95-103 (2007).

[21] A. Tilocca, Proceedings of The Royal Society A **465**, 1003-1027 (2009).

[22] J. K. Christie, and A. Tilocca, Chemistry of Materials **22**, 3725-3734 (2010).

[23] R. I. Ainsworth, D. Di Tommaso, J. K. Christie, and N. H. de Leeuw, The Journal of Chemical Physics **137**, 234502 (2012).

[24] J. K. Christie, R. I. Ainsworth, D. Di Tommaso, and N. H. de Leeuw, The Journal of Physical Chemistry B **117**, 10652-10657 (2013).

[25] M. Krack, and M. Parrinello, J. Grotendorst (Ed.), High Performance Computing in Chemistry **25**, 29-51 (2004).

[26] J. VandeVondele, M. Krack, F. Mohamed, M. Parrinello, T. Chassaing, and J. Hutter, Computer Physics Communications **167**, 103-128 (2005).

[27] CP2K developers group: `<http://www.cp2k.org>`; 2000-2013.

[28] G. Lippert, J. Hutter, and M. Parrinello, Molecular Physics: An International Journal at the Interface Between Chemistry and Physics **92**, 477-488 (1997).

[29] S. Goedecker, M. Teter, and J. Hutter, Physical Review B **54**, 1703-1710 (1996).

[30] C. Hartwigsen, S. Goedecker, and J. Hutter, Physical Review B **58**, 3641-3662 (1998).

[31] M. Krack, Theoretical Chemistry Accounts **114**, 145-152 (2005).

[32] J. P. Perdew, K. Burke, and M. Ernzerhof, Physical Review Letters **77**, 3865-3868 (1996).

[33] J. VandeVondele, and J. Hutter, The Journal of Chemical Physics **118**, 4365 (2003).

[34] R. S. Mulliken, The Journal of Chemical Physics **23**, 1833-1840 (1955).

[35] R. M. Moss, D. M. Pickup, I. Ahmed, J. C. Knowles, M. E. Smith, and R. J. Newport, Advanced Functional Materials **18**, 634-639 (2008).

[36] D. M. Pickup, I. Ahmed, P. Guerry, J. C. Knowles, M. E. Smith, and R. J. Newport, Journal of Physics-Condensed Matter **19**, 415116 (2007).

[37] S. M. Woodley, P. D. Battle, J. D. Gale, and C. R. A. Catlow, Physical Chemistry Chemical Physics **1**, 2535-2542 (1999).

[38] W. Smith, and T. R. Forester, Journal of Molecular Graphics **14**, 136-141 (1996).

[39] D. J. Evans, and G. P. Morriss, Computer Physics Reports **1**, 297-343 (1984).

[40] V. A. Bakaev, and W. A. Steele, The Journal of Chemical Physics **111**, 9803-9812 (1999).

[41] M. J. Sanders, M. Leslie, and C. R. A. Catlow, Journal of the Chemical Society-Chemical Communications **19**, 1271 (1984).

[42] A. Tilocca, N. H. de Leeuw, and A. N. Cormack, Physical Review B **73**, 104209 (2006).

[43] J. K. Christie, J. Malik, and A. Tilocca, Physical Chemistry Chemical Physics **13**, 17749 (2011).

[44] I. Ahmed, E. A. Abou Neel, S. P. Valappil, S. N. Nazhat, D. M. Pickup, D. Carta, D. L. Carroll, R. J. Newport, M. E. Smith, and J. C. Knowles, Journal of Materials Science **42**, 9827-9835 (2007).

[45] B. N. Mehrotra, T. Hahn, W. Eysel, H. Röpke, and A. Illguth, Neues Jahrbuch für Mineralogie, Monatshefte 408-421 (1978).

[46] J. C. Wasse, I. Petri, and P. S. Salmon, Journal of Physics-Condensed Matter **13**, 6165-6176 (2001).

[47] I. T. Penfold, and P. S. Salmon, Physical Review Letters **64**, 2164-2167 (1990).

[48] P. S. Salmon, S. Q. Xin, and H. E. Fischer, Physical Review B **58**, 6115-6123 (1998).

[49] J. Du, A. N. Cormack, Journal of Non-Crystalline Solids **349**, 66-79 (2004).

[50] J. F. Stebbins, Journal of Non-Crystalline Solids **106**, 359-369 (1988).

[51] M. Pota, A. Pedone, G. Malavasi, C. Durante, M. Cocchi, and M. C. Menziani, Computational Materials Science **47**, 739-751 (2010).

[52] Y. Kowada, H. Adachi, and T. Minami, Journal of Physical Chemistry **97**, 8989-8992 (1993).

[53] R. D. Shannon, Acta Crystallographica Section A **32**, 751-767 (1976).